RSC Advances

PAPER

View Article Online
View Journal | View Issue

Cite this: *RSC Adv.*, 2023, **13**, 11069

Improved redox synthesis of Mn–Co bimetallic oxide catalysts using citric acid and their toluene oxidation activity

Chongrui Xie,[a] Luming Li,[*b] Xuxu Zhai[c] and Wei Chu[*ac]

Received 3rd March 2023
Accepted 29th March 2023

DOI: 10.1039/d3ra01440a

rsc.li/rsc-advances

In this work, high-activity cobalt-doped α-MnO_2 hybrid materials were prepared using the citric acid oxidation reduction (CR) technique and applied to the catalytic oxidation of toluene. Compared to the traditional processes such as sol–gel, co-precipitation and our previous reported self-driving combustion process, the microstructure of Mn–Co bimetallic oxide catalyst is easier to regulated as well as the dispersion of active phase. Moreover, some accurate characterization techniques such as XRD, H_2-TPR, O_2-TPD, SEM, TEM, and XPS have been employed, to further illustrate the intrinsic factors for the efficient catalytic oxidation of toluene. It was ultimately found that the CR-Mn10Co1 prepared by citric acid oxidation reduction method could catalyze the oxidation of 90% of toluene at 232 °C, and its excellent catalytic performance was significantly related to its large specific surface area, excellent oxidation reduction ability, and abundant Mn^{3+} species and oxygen vacancy content. Therefore, citric acid oxidation reduction (CR) provides a convenient and effective route for the efficient and low-cost synthesis of Mn–Co catalysts for removing VOCs.

1 Introduction

Volatile Organic Compounds (VOCs) pose significant environmental and human health hazards, primarily contributing to ozone depletion, formation of photochemical smog, and elevated PM 2.5 levels.[1–3] The negative impact of VOCs emissions on human health, including the potential for disease and cancer, underscores the importance of controlling VOCs emissions.[4–6] In the search for effective and cost-efficient VOCs management strategies, catalytic combustion stands out as a promising option, offering superior treatment costs, degradation efficiency, and low secondary pollution.[7–10]

In recent years, catalysts employed for catalytic combustion of VOCs encompass supported precious metals, such as Pt,[11] Au,[12] Pd,[13] and Ag,[14] as well as transition metal oxides (TMOs).[3,15,16] Although supported noble metal catalysts display an outstanding reactivity, the scarcity and high cost of these precious metals hinder their practical application.[17,18] On the other hand, TMOs are abundant in mineral resources, and offer a cost-effective solution for VOCs catalytic combustion, but exhibit lower activity compared to noble metal catalysts. Among TMOs, manganese-, cobalt-, cerium-, and copper-oxide catalysts have exhibited potential for the degradation of VOCs, owing to their unique structure, valence states, and the presence of oxygen-enriched species on the surface. Developing an effective and low-cost method to synthesize TMO catalysts with high reactivity remains a crucial challenge in the degradation of VOCs.[19–21]

Recently the study of manganese-based catalysts in the context of transition metal oxide catalysts has garnered a significant amount of scholarly attention. This is due to manganese's low cost, abundant earth deposits, and its impressive catalytic properties, mixed valence, high lattice oxygen mobility, and the abundance of oxygen species on its surface.[21–24] Cobalt, as a transition metal, is also of interest due to its multiple oxide forms and abundant exposed crystal surfaces, as well as its demonstrated excellence in catalytic combustion of toluene.[25–28] The use of Mn–Co mixed oxide catalysts has shown an increase in toluene oxidation activity compared to single MnO_x or CoO_x catalysts, due to their synergism.[29–32] Xu *et al.*[33] evaluated the toluene degradation activity of Co–Mn composite oxide supported on nickel foam by hydrothermal synthesis method. The results showed that the high concentration of surface abundant oxygen vacancy defects, which played a crucial factor in enhancing the activity of toluene oxidation. Tang *et al.*[34] prepared Mn–Co composite oxide nanorods with multi-hole construction and high specific surface area by the oxalic acid method. Compared with the single manganese or cobalt-based catalyst, the manganese–cobalt mixed oxide catalysts showed enhanced activity for the oxidation of ethyl acetate and hexanes. Qu *et al.*[35] first prepared nanocrystalline Mn–Co catalysts with

[a]School of Chemical Engineering, Sichuan University, Chengdu 610065, China. E-mail: chuwei1965@scu.edu.cn
[b]College of Food and Biological Engineering, Chengdu University, Chengdu 610106, China. E-mail: liluming@cdu.edu.cn
[c]Institute of New Energy and Low Carbon Technology, Sichuan University, Chengdu 610207, China

a high pore size and large surface area using a two-step hydrothermal technique. The Mn–Co catalyst with an appropriate molar ratio of Mn/Co (1 : 2) achieved complete catalytic combustion of toluene at 250 °C. High porosity, large surface area and the unique structure of excellent oxygen species are the main reasons upon the enhanced the catalytic oxidation of toluene. Zhang *et al.*[36] synthesized bimetallic $MnCoO_x$ catalysts for the efficient synergistic ozone-catalyzed oxidation of chlorobenzene and NO in complex flue gases, which had excellent 3D spherical morphology, crystal structure, high porosity, and abundant acidity contributes to its excellent performance. Similarly, in the field of catalytic oxidation, the activation of molecular oxygen is an extremely important step, and the construction of a catalytic surface for the activation of molecular oxygen is essential.[37] Gu *et al.*[38] verified that a small amount of water enhances the catalytic oxidation of VOCs to transition metal oxides by activating lattice oxygen in the catalyst and forming hydroxyl species to attack the electron-deficient carbon in VOC. Montemore *et al.*[39] have addressed the process of oxygen activation on metal surfaces is a critical process for multiphase catalysis. Therefore, the construction of catalysts with unique structure, large specific surface area, excellent ability to activate oxygen molecules with lower valence of manganese species is crucial in the catalytic oxidation of VOCs in the design of manganese-based catalysts.

In this study, a novel and environmentally-friendly redox synthesis technique utilizing citric acid was developed for the preparation of one-step short rod-shaped α-MnO_2 hybrid composites doped with cobalt species. Co is added as a catalyst additive to enhance the stability and activity of the catalyst. The prepared Mn–Co catalysts were then compared with conventional preparation methods to assess the impact of different doping techniques on the uniform distribution and microstructure of the active phase. Through a comprehensive investigation, including X-ray diffraction (XRD), X-ray photoelectron spectroscopy (XPS), nitrogen adsorption and desorption, scanning and transmission electron microscopy (SEM and TEM), hydrogen-programmed temperature rises reduction (H_2-TPR), oxygen-programmed temperature rise desorption (O_2-TPD), and specific surface area testing (BET), the composition, structure, and redox performance of the Mn–Co catalysts were analyzed. The study also discussed the influence of different cobalt reference doses on the catalysts prepared by the citric acid oxidation–reduction method and described the internal factors that contribute to the efficient combustion of toluene.

2 Experimental

2.1 Preparation

2.1.1 Citric acid redox method (CR). In the process of citric acid redox synthesis, 4 g of potassium permanganate ($KMnO_4$) solid was dissolved in 100 mL of deionized water using ultrasonic oscillation for 30 minutes, resulting in solution I. Subsequently, 1.216 g of anhydrous citric acid and 0.631 g of cobalt acetate ($Co(CH_3COO)_2 \cdot 4H_2O$, Mn/Co = 10 : 1) were dissolved in 30 mL of deionized water and mixed *via* ultrasonic oscillation for 30 minutes to obtain solution II. At room temperature, solution I was slowly added to solution II at a rate of 2 drops per second, followed by reaction for 24 h at 50 °C. The resulting precipitate was filtered, washed with deionized water to neutralize, and dried at 100 °C for 12 h. The final product was designated as the CR-Mn10Co1 catalyst. By adjusting the Mn/Co ratio to 3 : 1, 5 : 1, 8 : 1, 13 : 1, and 15 : 1 and varying the amount of cobalt acetate, additional catalysts (CR-Mn3Co1, CR-Mn5Co1, CR-Mn8Co1, CR-Mn13Co1, and CR-Mn15Co1) were prepared with the same procedure. The process is illustrated in Scheme 1.

2.1.2 Citric acid sol–gel method (CS).[40] In the synthesis of the citric acid sol–gel method, a manganese nitrate solution with a mass fraction of 50% (10 g) and a $Co(NO_3)_2 \cdot 6H_2O$ solution (0.8132 g) were first dissolved in 30 mL of deionized water. Then, 7.085 g of citric acid (equivalent to 20% of the total cation

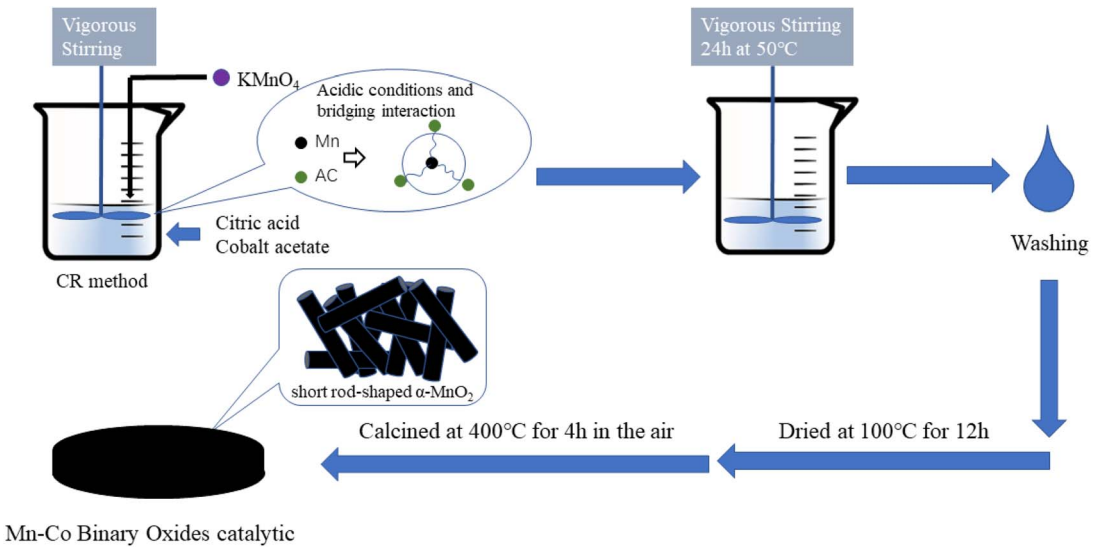

Scheme 1 Synthetic route of citric acid redox method.

moles) was added to the solution and fully dissolved through ultrasonic oscillation for 30 minutes. The solution was then concentrated and evaporated at 80 °C for 3 h, resulting in the formation of a sponge-like solid. The solid was dried overnight at 100 °C and then subjected to a temperature rise from room temperature to 400 °C at 5 °C per minute in a muffle furnace, where it was held for 4 hours to produce the CS-Mn10Co1 catalyst.

2.1.3 Co-precipitation method (CP).[41] In the co-precipitation synthesis process of the CP-Mn10Co1 catalyst, the process involved the dissolution of 10 g of manganese nitrate solution with a mass fraction of 50% and 0.8132 g of $Co(NO_3)_2 \cdot 6H_2O$ in 100 mL of deionized water. This solution was subjected to ultrasonic agitation for 30 minutes to fully dissolve the reagents and obtain solution III. Solution IV was obtained by adding 8.61 g of $NH_3 \cdot H_2O$ to 100 mL of deionized water. Solution IV was then slowly added to solution III with stirring, while maintaining a pH of 10. After the addition of solution IV was completed, the mixture was allowed to age for 24 h to obtain a stable product. The resulting precipitate was filtered, washed, and extracted three times with deionized water, and dried at 100 °C for 12 h. The sample was then subjected to thermal treatment in a muffle furnace by ramping up the temperature from room temperature to 400 °C at a rate of 5 °C min^{-1} and kept at this temperature for 4 hours to produce the CP-Mn10Co1 catalyst.

2.1.4 Self-driving combustion method (SDC).[42] In the synthesis process of the self-driving combustion method, 4 g of $KMnO_4$ was ground in an onyx grinding bowl. The resulting powder was then mixed with 0.6305 g of $Co(CH_3COO)_2 \cdot 6H_2O$, and the mixture was ground again until a smooth, fine powder was obtained. The mixture was then spread evenly onto a smooth quartz glass plate and ignited with a lighter. After the reaction was completed and the powder had cooled to room temperature, it was collected, washed with deionized water to neutral, and dried at 100 °C for 12 h to produce the SDC-Mn10Co1 catalyst.

2.2 Characterizations

The crystal structure and crystallinity of all catalysts were described by X-ray diffraction with the excitation source Cu Kα (λ = 1.542 Å). The equipment model was DX-2700B diffractometer, and the equipment used fixed parameters including a scanning range of 5° to 90° and a scanning speed of 0.05° per s.

N_2 adsorption–desorption curves were measured at liquid nitrogen temperature (77 K) using an automated specific surface area and pore size analyzer (Quantachrome NOVA 1000e device). Prior to testing, samples were degassed at 200 °C for 3 h under vacuum. The specific surface area of the catalyst was calculated by the BET equation and the pore volume and pore size distribution as well as the average pore size were calculated using the desorption curve according to the BJH method.

Scanning electron microscope (SEM) figure and transmission electron microscopy (TEM) figure were obtained using a ZEISS Gemini 300 scanning electron microscope and a FEI Tecnai G2 F20 instrument, respectively.

H_2-TPR test of all the samples was carried out on the TP-5080 instrument. During the hydrogen programmed temperature rise reduction (H_2-TPR), 30 mg of synthetic catalyst was used in a straight quartz reactor on a TCD chemisorption analyzer, followed by a 1 h N_2 stream pretreatment of the sample at 300 °C. After cool down to room temperature, the reducing gas (5% H_2/N_2) flows at a rate of 30 mL min^{-1} to a straight tube quartz reactor. The temperature procedure increases from 50 °C to 800 °C linearly at a speed of 10 °C min^{-1} and hydrogen consumption is instantaneously recorded by a TCD detector. O_2-TPD experiments were performed on the same chemisorption analyzer.

X-ray photoelectron spectroscopy (XPS) measurements of the prepared samples were performed using an Ultra DLD spectrometer, KRATOS, UK, using Al ka radiation ($h\nu$ = 1486.6 eV) as the radiation source.

2.3 Evaluation of toluene removal activity

In this study, the degradation of volatile organic compounds (VOCs) was investigated using toluene as a model reaction. A stainless-steel reaction tube, fitted with a quartz sand bed and a sample of catalyst (40–60 mesh) in the center to simulate a fixed-bed reactor, was placed in a heating furnace. The toluene feed gas, consisting of 1000 ppm toluene, 21% O_2, and N_2 (at equilibrium), was obtained by the foaming method at 0 °C and adjusted the concentration of air velocity. The total flow rate of the toluene feed gas was 50 mL min^{-1}, corresponding to a mass air velocity of GHSV = 30 000 mL $gcata^{-1}$ h^{-1}. Catalyst activation, eliminating any influence of the impurities trapped on the catalyst surface, the sample was pre-treated by heating to 300 °C for 60 minutes. After the pre-treatment, the furnace was cooled to 120 °C and maintained for over an hour to reach dynamic adsorption equilibrium for toluene in the bed. The reaction data were obtained by a gas chromatograph (SP-6890) with FID and TCD. The temperature was maintained at each test point for at least half an hour, and the data was recorded after reaching dynamic equilibrium to minimize errors. The toluene conversion ratio η% is computed as shown below:

$$\eta\% = \frac{N_{\mathrm{Tol,in}} - N_{\mathrm{Tol,out}}}{N_{\mathrm{Tol,in}}} \times 100\%$$

where $N_{\mathrm{Tol,in}}$ is the concentration of toluene entering the fixed-bed reactor, $N_{\mathrm{Tol,out}}$ is the concentration of the tail gas leaving the fixed-bed reactor after the reaction.

3 Results and discussion

3.1 Physical and structural properties of catalysts

In this study, the crystalline phase composition of catalysts prepared using four different methods was analyzed using XRD technique. It was displayed that the different crystal structures were presented vary with the prepared routes in Fig. 1(A). For CR-Mn10Co1, the XRD pattern is consistent with α-MnO_2 (PDF 44-0141), which has many acute and narrow diffraction peaks

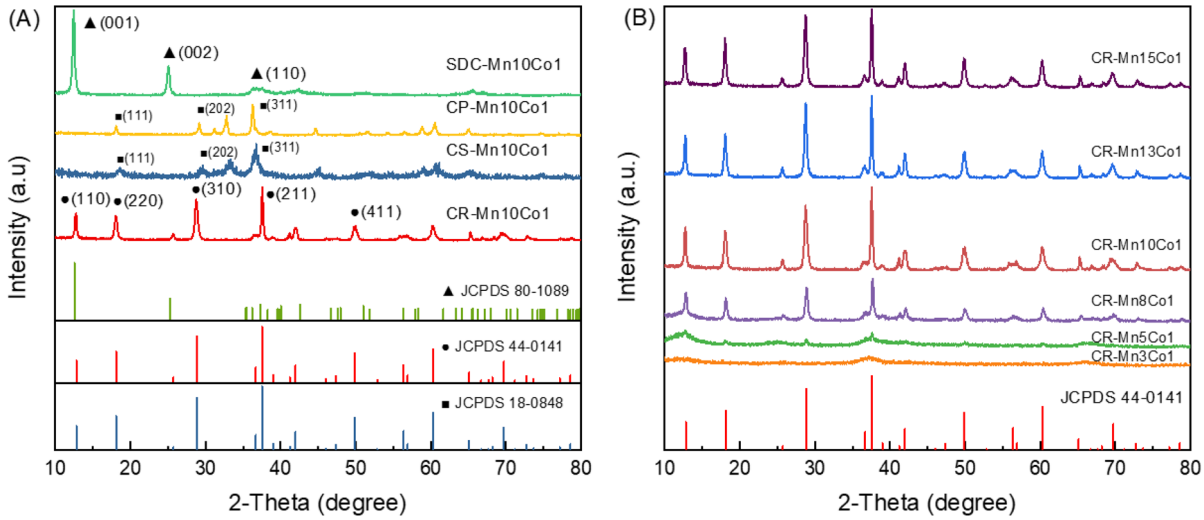

Fig. 1 (A) XRD patterns of as-prepared samples. (B) XRD patterns of CR-MnxCo1 samples.

indicating excellent crystallinity. The presence of this manganese oxide, which has a 2 × 2 tunneled [MnO_6] octahedral structure, is confirmed by the diffraction peaks at 2θ = 12.8°, 18.1°, 28.8°, 37.5°, 41.9°, 49.8°, and 60.3°.[43] Sample SDC-Mn10Co1 displays the diffraction peaks characteristic of birnessite manganese oxide phase δ-MnO_2 (PDF 80-1098), including peaks at 2θ = 12.4°, 25.1°, 37.3°, 42.6°, and 65.6°. This birnessite manganese oxide phase is formed through the violent combustion decomposition of $KMnO_4$ precursor.[42] The XRD pattern of sample CP-Mn10Co1 clearly shows the presence of spinel (Co, Mn)(Co, Mn)$_2O_4$ (PDF 18-0408), confirmed by the main peaks at 2θ = 18.2°, 29.4°, 32.9°, 38.8°, and 60.7°. This is also similarity for sample CS-Mn10Co1, which exhibits the same clear curve of spinel (Co, Mn)(Co, Mn)$_2O_4$.

The XRD profiles of a series of Mn-based catalysts prepared *via* the CR method with varying cobalt doping doses are shown in Fig. 1(B). For samples CR-Mn8Co1, CR-Mn10Co1, CR-Mn13Co1 and CR-Mn15Co1, the diffraction peaks at 2θ = 12.8° (110), 18.1° (200), 28.8° (310), 37.5° (211), 41.9° (301), 49.8° (411) and 60.3° (521) match those of α-MnO_2 (PDF 44-0141). As the cobalt doping dose increases, the diffraction peaks belonging to α-MnO_2 (PDF 44-0141) become weaker and less intense, as demonstrated by the decrease in intensity and smooth line segments of the diffraction peaks for CR-Mn3Co1 and CR-Mn5Co1. This trend suggests that the crystallinity of α-MnO_2 oxides decreases with increasing cobalt content, likely due to partial substitution of cobalt ions in the manganese octahedral lattice structure causing lattice expansion. This may result in the formation of a more amorphous structure.[29]

The specific surface area of all catalysts was evaluated using N_2 adsorption–desorption analysis. The results reveal a close association between the catalytic activity of the samples for toluene and their surface structure. The N_2 adsorption–desorption isotherms of the four catalysts (CR-Mn10Co1, CS-

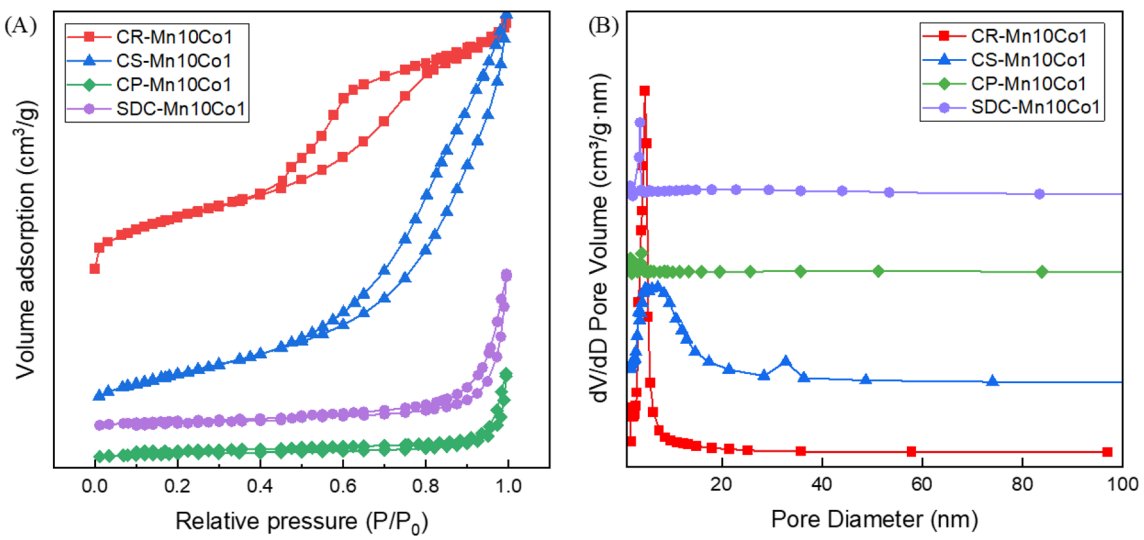

Fig. 2 (A) N_2 adsorption–desorption isotherms and (B) BJH pore-size distributions.

Table 1 Textural properties and catalytic activity of synthesized catalysts

		Textural property		
Sample	Mn/Co	S_{BET} (m^2 g^{-1})	Average pore diameter (nm)	Pore volume (cm^3 g^{-1})
CR-Mn10Co1	10 : 1	142.33	4.90	0.21
CS-Mn10Co1	10 : 1	96.59	8.90	0.30
CP-Mn10Co1	10 : 1	10.22	22.02	0.06
SDC-Mn10Co1	10 : 1	18.08	20.43	0.11
CR-Mn3Co1	3 : 1	28.13	22.92	0.17
CR-Mn5Co1	5 : 1	30.38	21.01	0.17
CR-Mn8Co1	8 : 1	61.29	19.71	0.17
CR-Mn13Co1	13 : 1	113.53	5.88	0.20
CR-Mn15Co1	15 : 1	79.52	10.32	0.22

Mn10Co1, CP-Mn10Co1, and SDC-Mn10Co1) are presented in Fig. 2(A), which were all categorized as classic type IV isotherms based on the IUPAC classification, which is usually the basis for judging the presence of mesopores in catalyst materials. The H3 hysteresis loops of the four samples show all relative pressures in the range of 0.4–1. The absence of adsorption saturation plateaus in the higher relative pressure range indicates that the presence of slits in the catalysts leads to irregularities in the pore structure. These two factors can be determined that an irregular mesopore is generated in the four catalysts.[29,44] The pore size distribution, shown in Fig. 2(B), was mainly distributed in the range of 1–40 nm, also confirming the presence of mesoporous structures in the catalysts.[41] The values of specific surface area, average pore size and pore volume of the catalysts are listed in Table 1. The lowest specific surface area of 10.2 m^2 g^{-1} was obtained for the CP-Mn10Co1 catalyst. CR-Mn10Co1 sample has the largest specific surface area (142.3 m^2 g^{-1}) and the smallest pore size (4.90 nm) indicates that the catalyst has a more abundant porous structure, which can facilitate the adsorption and diffusion of the reacting molecules, thus greatly reducing the hindrance of interphase mass transfer and enhancing its catalytic activity.[34] The magnitude of specific surface area of the catalysts varied in the order CR-Mn10Co1 (142.3 m^2 g^{-1}) > CS-Mn10Co1 (96.5 m^2 g^{-1}) > SDC-Mn10Co1 (18.8 m^2 g^{-1}) > CP-Mn10Co1 (10.2 m^2 g^{-1}). For the CR-derived catalysts with different Mn/Co ratios, the structural properties were observed to be closely linked to the Mn/Co ratios. SEM images revealed that the stacking of the rod-like manganese oxide was not complete at low Mn/Co doses due to poor crystallinity, resulting in a small specific surface area. However, at high Mn/Co ratios, the uniform short rods of manganese oxide stacked to form a porous coral-like structure. The increase in specific surface area was found to expose more active centers, enhance reactant adsorption and activation, and improve the catalytic performance,[45] which can explain the exceptional activity of the sample CR-Mn10Co1.

Table 2 XPS analysis results summary

	Mn		O	Catalytic activity (°C)	
Sample	Mn^{3+}/Mn^{4+}	AOS	O_{latt}/O_{ads}	T_{50}	T_{90}
CR-Mn10Co1	1.68	3.03	2.88	222	232
CS-Mn10Co1	1.6	3.44	1.72	239	257
CP-Mn10Co1	1.32	3.24	1.32	290	332
SDC-Mn10Co1	1.51	3.58	1.56	245	268

3.2 Catalytic oxidation performance of toluene

The catalytic activity of various samples was investigated through the catalytic combustion of toluene. The experiments were conducted at a toluene concentration of 1000 ppm, with a total flow rate of 50 mL min^{-1} and a resulting WHSV of 30 000 mL $gcata^{-1}$ h^{-1}, over a temperature range of 150 to 360 °C. The performance of the catalysts was evaluated based on T_{50} and T_{90} data, which indicate the temperatures at which 50%

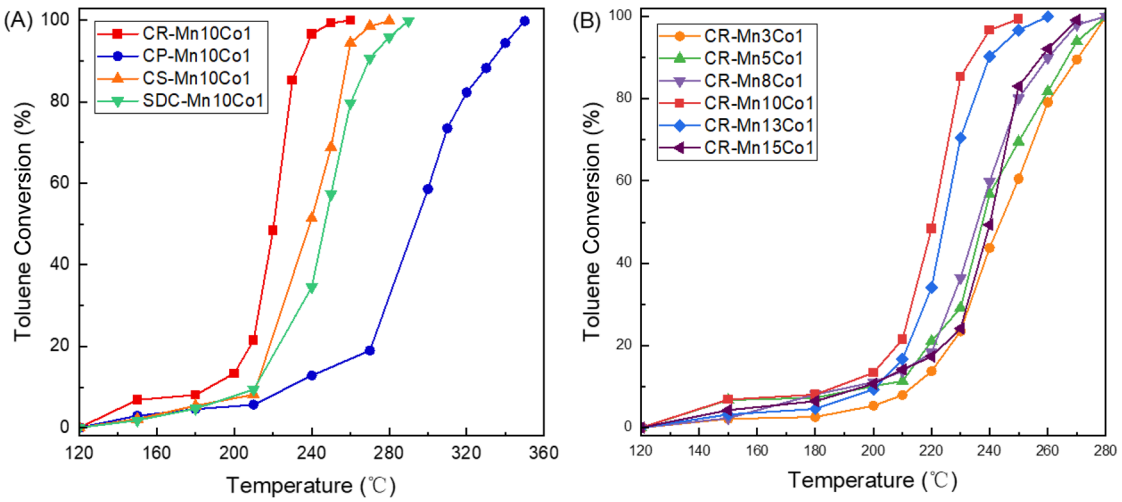

Fig. 3 (A) Toluene conversion *versus* reaction temperature over the different preparation methods. (B) Toluene conversion *versus* reaction temperature over the CR-MnxCo1 catalysts.

and 90% of the toluene was converted, respectively (see Table 2). As depicted in Fig. 3(A), the CR-Mn10Co1 sample displayed exceptional toluene removal performance compared to the catalysts produced through other preparation methods. The sample achieved T_{50} at 222 °C and T_{90} at 232 °C, which is attributed to its high specific surface area and unique hollow α-MnO_2 tunneling structure. XPS results further indicated that the CR-Mn10Co1 sample had the highest Mn^{3+} ratio and the largest lattice oxygen ratio, contributing to its exceptional performance in toluene combustion.

Fig. 3(B) presents a comparison of the toluene oxidation activity of catalysts with varying cobalt doping concentrations. The results demonstrate that the activity of the catalyst prepared *via* citric acid redox method is influenced by the amount of cobalt doping, with the best performance observed for the Mn/Co ratio of 10 : 1. This sample achieved complete toluene conversion at 240 °C, with T_{50} and T_{90} values of 222 °C and 232 °C, respectively, which may be associated with its specific surface area and crystal size. In contrast, as the Mn/Co ratio decreased, the catalyst activity decreased correspondingly, with the lowest activity achieved for the CR-Mn3Co1 catalyst with T_{50} and T_{90} values of 243 °C and 271 °C, respectively. The observed performance trend, CR-Mn10Co1 > CR-Mn13Co1 > CR-Mn15Co1 > CR-Mn8Co1 > CR-Mn5Co1 > CR-Mn3Co1, indicates that the content of the doped metal elements has a significant impact on the performance of manganese-based catalysts in the catalytic combustion of toluene. Furthermore, low cobalt oxide content is beneficial for improved catalytic performance. The XRD and SEM results suggest that the addition of large amounts of cobalt species leads to the formation of large grain size, which obstructs the active sites of the catalyst and reduces the crystallinity of α-MnO_2, ultimately decreasing the catalyst activity.

3.3 Morphology and redox properties of samples

The morphological structures of the catalytic samples were examined using scanning electron microscopy (SEM). Fig. 4 displays the SEM images of the samples produced by four preparation methods. The sample CR-Mn10Co1 exhibited a loose, porous, coral-like structure under electron microscopy. Upon closer examination, this coral-like structure was found to consist of many nano-rod-like structures, each 20 nm in diameter and 200–400 nm in length. The sample CS-Mn10Co1 showed a porous, sparse, cheese-like microstructure under SEM. The CP-Mn10Co1 mixed oxide catalyst had a nanosphere-like structure. The SDC-Mn10Co1 sample exhibited a nanosheet-like layered structure, typical of δ-MnO_2, with these sheets randomly stacked and overlapped with each other. The microstructural features of the samples prepared *via* the citric acid redox method with varying cobalt doping levels were analyzed using scanning electron microscopy and are presented in Fig. 5. The SEM images reveal a clear correlation between the cobalt doping level and the microstructure of the samples. Samples CR-Mn3Co1 and CR-Mn5Co1, with high cobalt loading, display an intermingled aggregation of irregular spheres and blocks, suggesting that the pore structure is not fully exposed and that the surface area available for reaction is relatively small, in agreement with the specific surface area measurements. With decreasing cobalt doping, the CR-Mn8Co1 sample exhibits a growing abundance of fine rod-like α-MnO_2 structures. This trend continues as cobalt doping is further decreased in samples CR-Mn10Co1 and CR-Mn13Co1, which

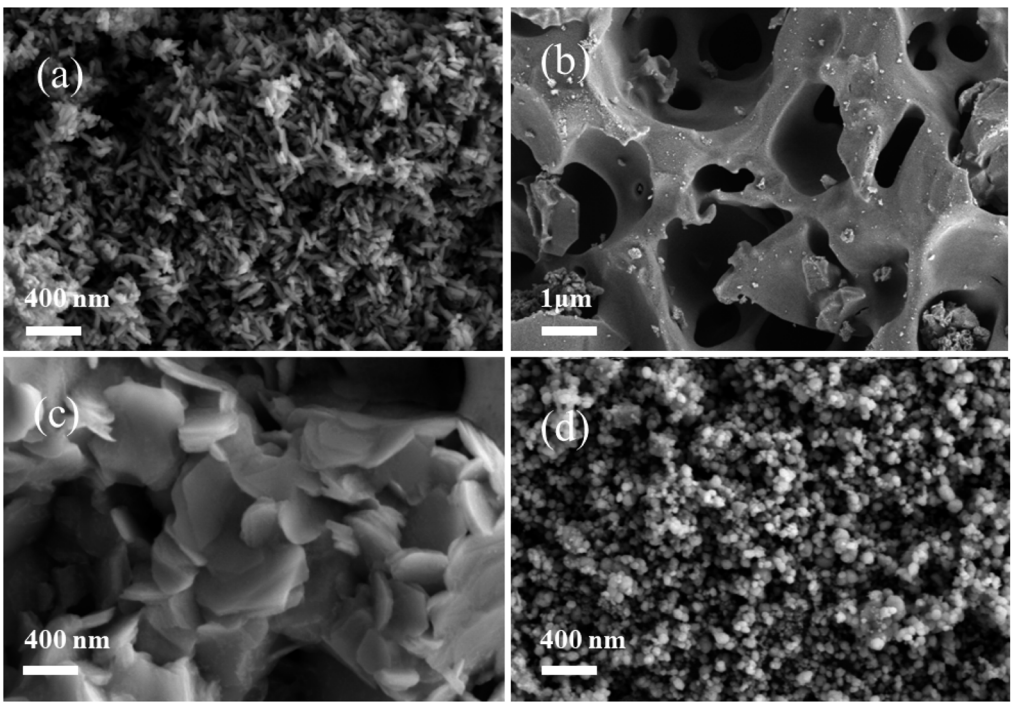

Fig. 4 SEM images of (a) CR-Mn10Co1; (b) CS-Mn10Co1; (c) SDC-Mn10Co1; (d) CP-Mn10Co1.

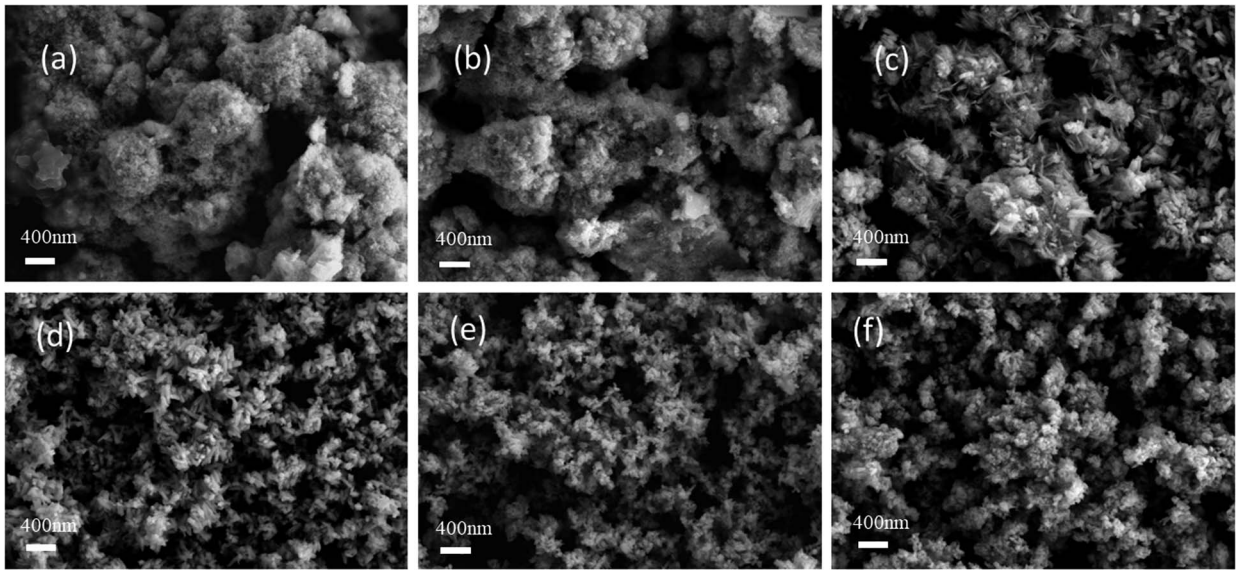

Fig. 5 SEM images of (a) CR-Mn3Co1; (b) CR-Mn5Co1; (c) CR-Mn8Co1; (d) CR-Mn10Co1; (e) CR-Mn13Co1; (f) CR-Mn15Co1.

exhibit homogeneous, loose, and porous micro-rod-like structures with increased porosity and surface area. However, when the Mn/Co ratio exceeds 10, as in the CR-Mn15Co1 sample, the micro-rod-like structure is not fully developed, leading to reduced catalytic surface area and a decrease in activity. It is proposed that this phenomenon may be due to the strong oxidizing property of potassium permanganate in the citric acid redox method, and that reducing the amount of cobalt acetate reducing agent may promote a gentler redox reaction and result in more uniform growth of micro-rod α-MnO_2.

The nanostructure of the CR-Mn10Co1 mixed oxide catalyst, which exhibited the best catalytic performance among the samples studied, was further investigated *via* transmission electron microscopy (TEM) analysis, as depicted in Fig. 6. The TEM images of CR-Mn10Co1 revealed a microstructure composed of nanorod-like structures stacked upon each other, exhibiting a rectangular shape with a clear lateral structure. The α-MnO_2 phase typically grows along the [001] direction orientation (*c*-axis), resulting in the four sidewalls being the primary exposed surfaces.[43] The TEM images reveal a microstructure of nano-rod-like structures stacked upon one another, with a rectangular shape and a distinct lateral structure. High magnification observations show that the lattice spacings of 4.4 Å and 3.1 Å on the exposed crystal faces of the sidewalls correspond to the (200) and (310) crystal faces of α-MnO_2, respectively, as confirmed by X-ray diffraction analysis. The literature suggests that the exposure of the high-index (310) crystal plane may enhance the catalytic activity of the sample.[43] This correlation with the crystal plane may provide insight into the exceptional activity of the CR-Mn10Co1 catalyst.

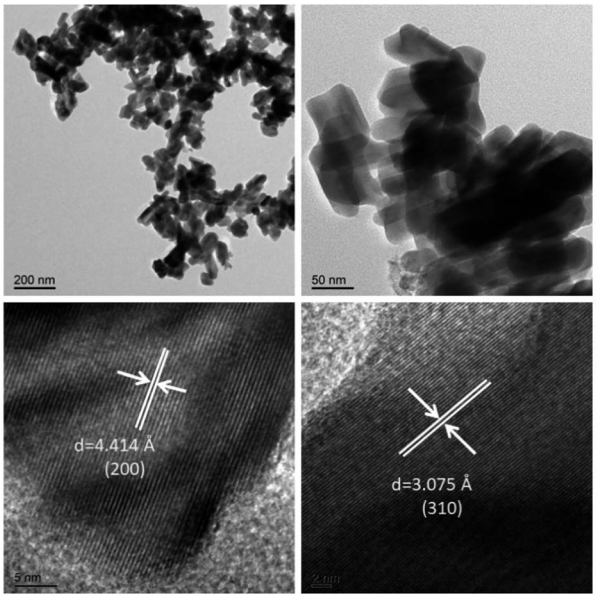

Fig. 6 TEM images of CR-Mn10Co1 catalyst.

The hydrogen temperature-programmed reduction (H_2-TPR) experiment was employed to assess the redox performance and mobility of oxygen in the prepared catalysts. The H_2-TPR curves of the catalysts prepared by the four methods are shown in Fig. 7(A). All four samples from different preparation methods showed a typical two-step reduction process of MnO_2, which could correspond to the reduction paths of $Mn^{4+} \rightarrow Mn^{3+}$ and $Mn^{3+} \rightarrow Mn^{2+}$.[35,46] For sample CR-Mn10Co1, the reduction process only has a broad overlapping peak at 351 °C. The rapid reduction process and the merging of the two reduction peaks demonstrate the sample's exceptional low-temperature reduction ability, attributed to the presence of potassium in the precursor which facilitates the reduction of MnO_2 to MnO and increases the surface reactivity of oxygen species, ultimately leading to high activity.[47] For the sample SDC-Mn10Co1, there are two broad overlapping reduction peaks at 359 °C and 429 °C, which are second only to CR-Mn10Co1 in terms of low-temperature and high-temperature reduction peaks compared

with the catalysts prepared by other methods. For the sample CS-Mn10Co1, there are two broad reduction peaks at 336 °C and 453 °C. For CP-Mn10Co1, there are two broader and weaker reduction peaks at 468 °C and 527 °C. The relatively high reduction temperature of the manganese-based catalysts indicates a relatively strong Mn–O bond, which may suppress the involvement of reactive oxygen in the reaction, while the relatively low reduction temperature implies a faster movement of lattice oxygen to the surface, demonstrating a favourable oxygen mobility.

O_2-TPD analysis was used to study the oxygen species and oxygen desorption behavior of mixed oxide catalysts. O_2-TPD experiments were performed on the catalyst samples prepared by the four methods to analyze the oxygen species of the prepared catalysts. The O_2-TPD curves are shown in Fig. 7(B). The desorbed O_2 species below 300 °C are surface adsorbed oxygen (O_{low}) on the catalyst surface; those desorbed within 300–600 °C are called subsurface lattice oxygen (O_{mid}); above 600 °C usually appear as bulk phase lattice oxygen (O_{high}).[48] Fig. 7(B) demonstrates varied oxygen desorption behaviors among four samples. Specifically, CS-Mn10Co1 exhibited the most abundant oxygen species, however, the primary adsorbed oxygen species were predominantly found in the bulk phase lattice oxygen. In contrast, CR-Mn10Co1 exhibited rich oxygen species concentration and comprised both surface lattice oxygen and bulk phase lattice oxygen. Additionally, both SDC-Mn10Co1 and CP-Mn10Co1 samples demonstrated comparable distributions of total oxygen species, which were mainly comprised of surface lattice oxygen with an amount of adsorbed oxygen, but did not exhibit good activity. Based on these outcomes, it can be inferred that lattice oxygen plays a crucial role in the catalytic oxidation of toluene, aligning with the MVK mechanism commonly reported in literature.[15,49] This mechanism proposes that toluene molecules first adsorb on active sites of the catalyst and then react with adjacent lattice oxygen, forming CO_2, H_2O, and oxygen vacancies. These vacancies are subsequently replenished by oxygen molecules present in the gas phase, resulting in a redox cycle and formation of lattice oxygen.[50,51] In short, it is evident that the CR-Mn10Co1 catalyst, due to its rich concentration of oxygen vacancies, excellent lattice oxygen concentration, and mobility, plays a critical role in enhancing the oxidation capacity of toluene.

3.4 Surface physical and chemical property analysis

The surface composition and chemical state of the catalysts were characterized using X-ray photoelectron spectroscopy (XPS). Fig. 8 displays the Mn $2p_{3/2}$, Mn 3s, and O 1s spectra for the four samples, the key active elements. The distribution of various manganese valences and the average oxidation state (AOS) of the catalyst were determined by fitting the curves, as displayed in Table 2. The analysis yielded information on the concentration of different oxygen species and the relative content of various valence manganese elements.

The Mn 2p spectrum of each sample was successfully decomposed into two regions, characterized by binding energies ranging from 643.1 to 643.7 eV and from 641.5 to 641.9 eV, corresponding to Mn^{4+} and Mn^{3+} ions, respectively.[52,53] It was clearly observed that the Mn^{3+} content of catalysts prepared *via* different methods displayed significant variations, with the order of CR-Mn10Co1 > CS-Mn10Co1 > SDC-Mn10Co1 > CP-Mn10Co1. Notably, the CR-Mn10Co1 catalyst exhibited the highest Mn^{3+}/Mn^{4+} ratio (1.68) among the four samples. As per the literature, a higher Mn^{3+} content in a catalyst is associated with an increased number of defects and oxygen vacancies, due to electrostatic equilibrium effects. The higher Mn^{3+} ratio implies a higher concentration of oxygen vacancies, which play a crucial role as the active center in oxidation reactions. The highest Mn^{3+} ratio observed in CR-Mn10Co1 indicates the presence of a greater quantity of oxygen vacancies, leading to an increased generation of oxygen vacancies to maintain charge balance when more Mn^{3+} is generated in the catalyst due to the charge compensation mechanism.[54]

$$-Mn^{4+}-O^{2-}-Mn^{4+}-\rightarrow -Mn^{3+}-\square -Mn^{3+}- +\frac{1}{2}O_2$$

The □ in the formula represents the oxygen vacancy of the manganese based catalyst.[55] The CR-Mn10Co1 catalyst

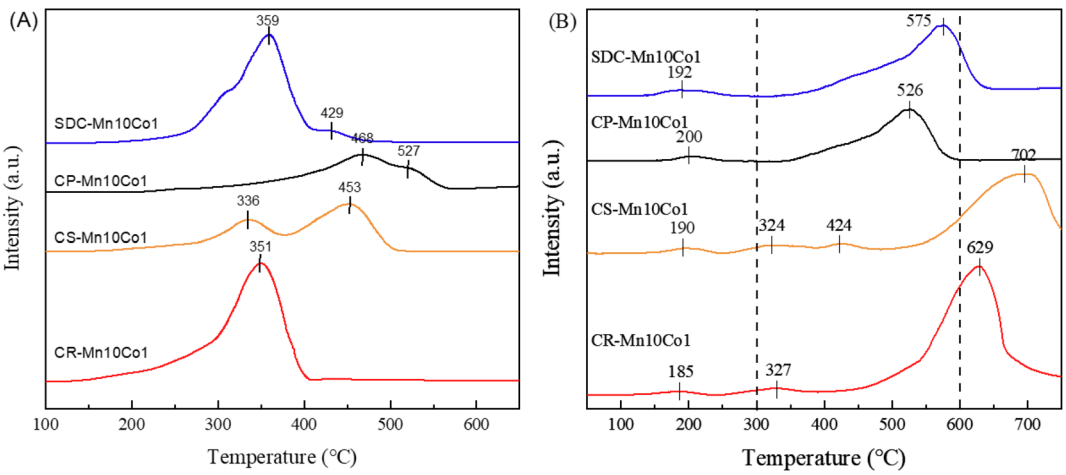

Fig. 7 H_2-TPR (A) and O_2-TPD (B) images of four catalysts.

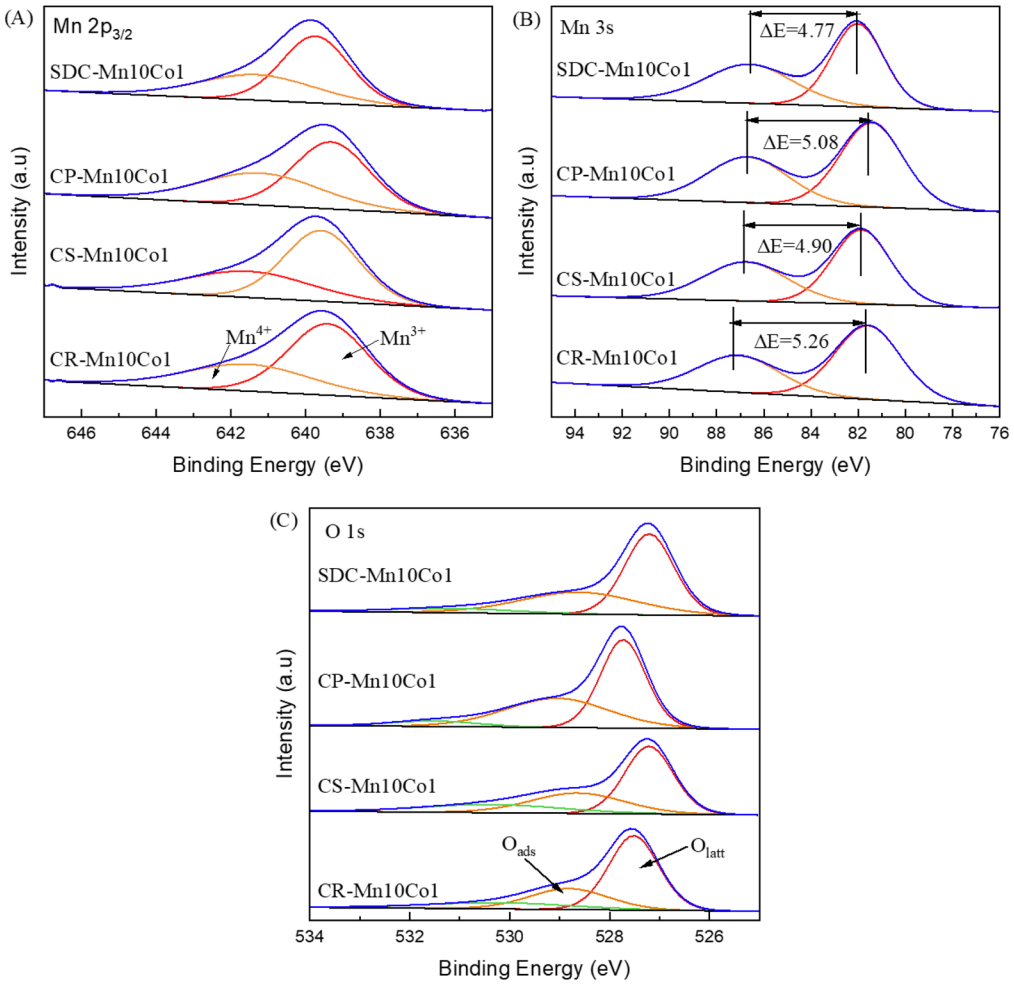

Fig. 8 XPS spectra of (A) Mn $2p_{3/2}$, (B) Mn 3s, (C) O 1s over CR, CS, CP and SDC-Mn10Co1.

exhibited the highest concentration of surface oxygen vacancies, enabling it to adsorb and convert a greater quantity of gaseous oxygen and thus demonstrating a stronger capability to replenish gaseous O_2 as compared to the other three catalysts. In conclusion, the exceptional activity of the CR-Mn10Co1 catalyst can be attributed to its superior active oxygen mobility, arising from its inherent heterogeneity in crystal tunneling. This heterogeneity leads to the formation of more Mn^{3+} ions with oxygen vacancies on the surface, resulting in exceptional catalytic activity.

The average oxidation state (AOS) of all samples was calculated from the spectrogram of Mn 3s.[56] The AOS of Mn varied as follows: SDC-Mn10Co1(3.58) > CS-Mn10Co1(3.44) > CP-Mn10Co1(3.24) > CR-Mn10Co1(2.88). The lower the AOS, the higher the amount of Mn^{3+} represented. AOS computed by the below equation: $AOS = 8.956 - 1.126 \times \Delta E$.

The O 1s spectra of the samples under investigation were meticulously fitted to three distinct energy regions, characterized by binding energies of 529.1 to 529.3 eV, 530.9 to 531.1 eV, and 532.9 eV. These regions correspond to lattice oxygen (O_{latt}), oxygen species adsorbed on the surface (O_{ads}), and hydroxyl oxygen in chemically-bound water ($O_{adsO\text{-}H}$), respectively.[57–59] The Mars–van Krevelen mechanism(MVK) posits that an increase in the number of oxygen vacancies can boost the mobility of oxygen species and that a higher lattice-to-adsorbed oxygen ratio (O_{latt}/O_{ads}) can facilitate the catalytic oxidation process of toluene, thereby enhancing the catalyst's performance.[46,49] Our analysis of four samples, namely CS-Mn10Co1, CP-Mn10Co1, SDC-Mn10Co1, and CR-Mn10Co1, supports this hypothesis. The O_{latt}/O_{ads} ratios of CS-Mn10Co1, CP-Mn10Co1, and SDC-Mn10Co1 were found to be 1.72, 1.32, and 1.56, respectively, and these values were consistent with the observed catalytic performance. Notably, CR-Mn10Co1, which exhibited the best catalytic activity, had the lowest amount of adsorbed oxygen species (3.03) and the highest O_{latt}/O_{ads} ratio (2.88) compared to Mn–Co catalysts produced using other conventional methods. These results provide compelling evidence for the involvement of oxygen vacancies and lattice oxygen at the surface in the catalytic combustion of toluene.

3.5 Stability test

The performance of the CR-Mn10Co1 sample, synthesized by the citric acid redox method, was evaluated for its industrial utility through multiple cycles of use and a stability test. The

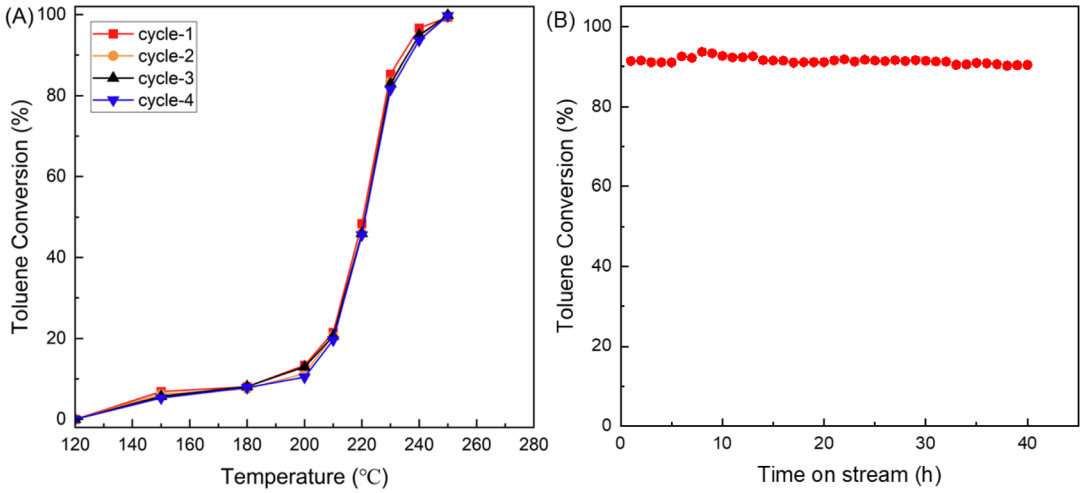

Fig. 9 (A) Cyclical stability test of CR-Mn10Co1 catalyst over toluene conversion. (B) Toluene conversion *vs.* reaction time over CR-Mn10Co1 under 40 h continuous test.

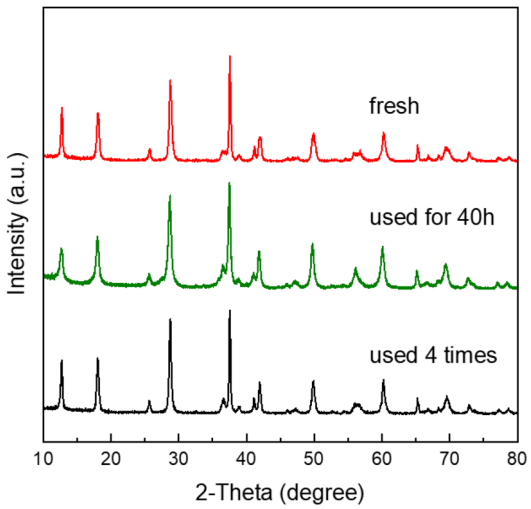

Fig. 10 Comparison of XRD patterns of CR-Mn10Co1 sample before and after use.

results, presented in Fig. 9, showed that the sample had exceptional recycling performance with consistent toluene conversion over four reaction cycles at a mass vacancy rate of 30 000 mL gcata^{-1} h^{-1}. The 40 hours stability test further revealed that the toluene conversion of the CR-Mn10Co1 remained stable at over 90% during the entire reaction, even at a temperature of 232 °C. Meanwhile, by XRD characterization tests of the samples before and after the reaction as shown in Fig. 10, it was found that the crystalline phase of the samples remained stable after 40 h of stability tests with four cyclicity tests. We can deduce that this stability is attributed to the sample's ability to recycle oxygen species, which can be replenished by gas-phase oxygen as it is consumed. The results demonstrate the potential industrial application of the CR-Mn10Co1 sample as a highly stable catalyst.

4 Conclusions

The citric acid redox method was used to synthesize a CoO_2/α-MnO_2 mixed oxide catalyst with a single-crystal structure and abundant oxygen vacancies. Results indicate that this catalyst has superior structure and performance compared to catalysts prepared using other methods. The doping level of cobalt additive was found to significantly impact the specific surface area, crystalline structure, and morphological features of the catalysts. Among the prepared catalysts, the CR-Mn10Co1 catalyst exhibited the highest catalytic activity for the oxidation of toluene, with 90% conversion at 232 °C. This was linked to its larger specific surface area, exceptional redox properties, numerous oxygen vacancies, and high concentration of Mn^{3+} species. This study offers insights into the development of highly active Mn–Co catalysts for the removal of volatile organic compounds.

Conflicts of interest

There are no conflicts to declare.

Acknowledgements

This work was supported by a grant from the National Natural Science Foundation of China (21872098).

Notes and references

1 A. Mellouki, T. J. Wallington and J. Chen, *Chem. Rev.*, 2015, **115**, 3984–4014.
2 M. S. Kamal, S. A. Razzak and M. M. Hossain, *Atmos. Environ.*, 2016, **140**, 117–134.
3 C. He, J. Cheng, X. Zhang, M. Douthwaite, S. Pattisson and Z. Hao, *Chem. Rev.*, 2019, **119**, 4471–4568.
4 R. J. Huang, Y. Zhang, C. Bozzetti, K. F. Ho, J. J. Cao, Y. Han, K. R. Daellenbach, J. G. Slowik, S. M. Platt, F. Canonaco,

P. Zotter, R. Wolf, S. M. Pieber, E. A. Bruns, M. Crippa, G. Ciarelli, A. Piazzalunga, M. Schwikowski, G. Abbaszade, J. Schnelle-Kreis, R. Zimmermann, Z. An, S. Szidat, U. Baltensperger, I. El Haddad and A. S. Prevot, *Nature*, 2014, **514**, 218–222.

5 M. Ehn, J. A. Thornton, E. Kleist, M. Sipila, H. Junninen, I. Pullinen, M. Springer, F. Rubach, R. Tillmann, B. Lee, F. Lopez-Hilfiker, S. Andres, I. H. Acir, M. Rissanen, T. Jokinen, S. Schobesberger, J. Kangasluoma, J. Kontkanen, T. Nieminen, T. Kurten, L. B. Nielsen, S. Jorgensen, H. G. Kjaergaard, M. Canagaratna, M. D. Maso, T. Berndt, T. Petaja, A. Wahner, V. M. Kerminen, M. Kulmala, D. R. Worsnop, J. Wildt and T. F. Mentel, *Nature*, 2014, **506**, 476–479.

6 U. Poschl and M. Shiraiwa, *Chem. Rev.*, 2015, **115**, 4440–4475.

7 Y. Guo, M. Wen, G. Li and T. An, *Appl. Catal., B*, 2021, **281**, 119447.

8 C. Yang, G. Miao, Y. Pi, Q. Xia, J. Wu, Z. Li and J. Xiao, *Chem. Eng. J.*, 2019, **370**, 1128–1153.

9 L. F. Liotta, *Appl. Catal., B*, 2010, **100**, 403–412.

10 M. J. Hülsey, S. Baskaran, S. Ding, S. Wang, H. Asakura, S. Furukawa, S. Xi, Q. Yu, C.-Q. Xu, J. Li and N. Yan, *CCS Chem.*, 2022, **4**, 3296–3308.

11 S. Ding, H.-A. Chen, O. Mekasuwandumrong, M. J. Hülsey, X. Fu, Q. He, J. Panpranot, C.-M. Yang and N. Yan, *Appl. Catal., B*, 2021, **281**, 119471.

12 J. Chen, M. Jiang, J. Chen, W. Xu and H. Jia, *J. Hazard. Mater.*, 2020, **392**, 122511.

13 Y. Guo, Y. Gao, X. Li, G. Zhuang, K. Wang, Y. Zheng, D. Sun, J. Huang and Q. Li, *Chem. Eng. J.*, 2019, **362**, 41–52.

14 H. Yang, J. Deng, Y. Liu, S. Xie, Z. Wu and H. Dai, *J. Mol. Catal. A: Chem.*, 2016, **414**, 9–18.

15 G. Li, N. Li, Y. Sun, Y. Qu, Z. Jiang, Z. Zhao, Z. Zhang, J. Cheng and Z. Hao, *Appl. Catal., B*, 2021, **282**, 119512.

16 S. Scirè and L. F. Liotta, *Appl. Catal., B*, 2012, **125**, 222–246.

17 J. Fan, Y. Sun, M. Fu, J. Li and D. Ye, *J. Hazard. Mater.*, 2022, **424**, 127505.

18 C. He, Y. Liao, C. Chen, D. Xia, Y. Wang, S. Tian, J. Yang and D. Shu, *Appl. Catal., B*, 2022, **303**, 120881.

19 Q. Huang, Z.-Y. Zhang, W.-J. Ma, Y.-W. Chen, S.-M. Zhu and S.-B. Shen, *J. Ind. Eng. Chem.*, 2012, **18**, 757–762.

20 Y. Zeng, K. G. Haw, Z. Wang, Y. Wang, S. Zhang, P. Hongmanorom, Q. Zhong and S. Kawi, *J. Hazard. Mater.*, 2021, **404**, 124088.

21 P. Gong, F. He, J. Xie and D. Fang, *Chemosphere*, 2023, **318**, 137938.

22 J. Li, L. Li, F. Wu, L. Zhang and X. Liu, *Catal. Commun.*, 2013, **31**, 52–56.

23 L. Lamaita, M. A. Peluso, J. E. Sambeth and H. J. Thomas, *Appl. Catal., B*, 2005, **61**, 114–119.

24 S. Mo, Q. Zhang, J. Li, Y. Sun, Q. Ren, S. Zou, Q. Zhang, J. Lu, M. Fu, D. Mo, J. Wu, H. Huang and D. Ye, *Appl. Catal., B*, 2020, **264**, 118464.

25 S. Zhao, T. Li, J. Lin, P. Wu, Y. Li, A. Li, T. Chen, Y. Zhao, G. Chen, L. Yang, Y. Meng, X. Jin, Y. Qiu and D. Ye, *Chem. Eng. J.*, 2021, **420**, 130448.

26 L. F. Liotta, H. Wu, G. Pantaleo and A. M. Venezia, *Catal. Sci. Technol.*, 2013, **3**, 3085.

27 Y. Wang, H. Arandiyan, Y. Liu, Y. Liang, Y. Peng, S. Bartlett, H. Dai, S. Rostamnia and J. Li, *ChemCatChem*, 2018, **10**, 3429–3434.

28 S. Todorova, H. Kolev, J. P. Holgado, G. Kadinov, C. Bonev, R. Pereñíguez and A. Caballero, *Appl. Catal., B*, 2010, **94**, 46–54.

29 P. Wang, J. Wang, X. An, J. Shi, W. Shangguan, X. Hao, G. Xu, B. Tang, A. Abudula and G. Guan, *Appl. Catal., B*, 2021, **282**, 119560.

30 Q. Zhang, X. Liu, W. Fan and Y. Wang, *Appl. Catal., B*, 2011, **102**, 207–214.

31 D. A. Aguilera, A. Perez, R. Molina and S. Moreno, *Appl. Catal., B*, 2011, **104**, 144–150.

32 B. Faure and P. Alphonse, *Appl. Catal., B*, 2016, **180**, 715–725.

33 X. Jiang, W. Xu, S. Lai and X. Chen, *RSC Adv.*, 2019, **9**, 6533–6541.

34 W. Tang, X. Wu, S. Li, W. Li and Y. Chen, *Catal. Commun.*, 2014, **56**, 134–138.

35 Z. Qu, K. Gao, Q. Fu and Y. Qin, *Catal. Commun.*, 2014, **52**, 31–35.

36 Z. Zhang, F. Lin, L. Xiang, H. Yu, Z. Wang, B. Yan and G. Chen, *Chem. Eng. J.*, 2022, **427**, 130929.

37 Z. Wang, M. Cheng, Y. Liu, Z. Wu, H. Gu, Y. Huang, L. Zhang and X. Liu, *Angew. Chem., Int. Ed. Engl.*, 2023, e202301483, DOI: **10.1002/anie.202301483**.

38 H. Gu, J. Lan, Y. Liu, C. Ling, K. Wei, G. Zhan, F. Guo, F. Jia, Z. Ai, L. Zhang and X. Liu, *ACS Catal.*, 2022, **12**, 11272–11280.

39 M. M. Montemore, M. A. van Spronsen, R. J. Madix and C. M. Friend, *Chem. Rev.*, 2018, **118**, 2816–2862.

40 J. Yang, L. Li, X. Yang, S. Song, J. Li, F. Jing and W. Chu, *Catal. Today*, 2019, **327**, 19–27.

41 X. Huang, L. Li, R. Liu, H. Li, L. Lan and W. Zhou, *Catalysts*, 2021, **11**, 1037.

42 X. Zhai, F. Jing, L. Li, X. Jiang, J. Zhang, J. Ma and W. Chu, *Fuel*, 2021, **283**, 118888.

43 S. Rong, P. Zhang, F. Liu and Y. Yang, *ACS Catal.*, 2018, **8**, 3435–3446.

44 N. Huang, Z. Qu, C. Dong, Y. Qin and X. Duan, *Appl. Catal., A*, 2018, **560**, 195–205.

45 Y. Xu, Z. Qu, Y. Ren and C. Dong, *Appl. Surf. Sci.*, 2021, **560**, 139983.

46 H. Sun, Z. Liu, S. Chen and X. Quan, *Chem. Eng. J.*, 2015, **270**, 58–65.

47 W. Yang, Z. A. Su, Z. Xu, W. Yang, Y. Peng and J. Li, *Appl. Catal., B*, 2020, **260**, 118150.

48 W. Yang, Y. Peng, Y. Wang, Y. Wang, H. Liu, Z. A. Su, W. Yang, J. Chen, W. Si and J. Li, *Appl. Catal., B*, 2020, **278**, 119279.

49 X. Zhai, L. Li, S. Song, J. Zhang, J. Ma, C. Xie and W. Chu, *Fuel*, 2023, **334**, 126780.

50 X. L. Li, Y. F. Niu, C. A. W. Zhang, H. G. Su and Y. X. Qi, *Chemcatchem*, 2021, **13**, 4223–4236.
51 Z. Su, W. Si, H. Liu, S. Xiong, X. Chu, W. Yang, Y. Peng, J. Chen, X. Cao and J. Li, *Environ. Sci. Technol.*, 2021, **55**, 12630–12639.
52 S. Mo, S. Li, W. Li, J. Li, J. Chen and Y. Chen, *J. Mater. Chem. A*, 2016, **4**, 8113–8122.
53 Y. Lyu, C. Li, X. Du, Y. Zhu, Y. Zhang and S. Li, *Fuel*, 2020, **262**, 116610.
54 Y. Wang, J. Wu, G. Wang, D. Yang, T. Ishihara and L. Guo, *Appl. Catal., B*, 2021, **285**, 119873.
55 J. Hou, Y. Li, L. Liu, L. Ren and X. Zhao, *J. Mater. Chem. A*, 2013, **1**, 2736.
56 Y. Sun, X. Zhang, N. Li, X. Xing, H. Yang, F. Zhang, J. Cheng, Z. Zhang and Z. Hao, *Appl. Catal., B*, 2019, **251**, 295–304.
57 J. Zhang, Y. Li, L. Wang, C. Zhang and H. He, *Catal. Sci. Technol.*, 2015, **5**, 2305–2313.
58 J. Wang, J. Li, C. Jiang, P. Zhou, P. Zhang and J. Yu, *Appl. Catal., B*, 2017, **204**, 147–155.
59 V. P. Santos, M. F. R. Pereira, J. J. M. Órfão and J. L. Figueiredo, *Appl. Catal., B*, 2010, **99**, 353–363.